

Synthesis, characterization and activity pattern of Cu–ZnO/ZrO₂ catalysts in the hydrogenation of carbon dioxide to methanol

Francesco Arena^{a,b,*}, Katia Barbera^a, Giuseppe Italiano^a, Giuseppe Bonura^b, Lorenzo Spadaro^b,
Francesco Frusteri^b

^a Dipartimento di Chimica Industriale e Ingegneria dei Materiali, Università degli Studi di Messina, Salita Sperone 31 c.p. 29, I-98166 S. Agata (Messina), Italy

^b Istituto CNR-ITAE “Nicola Giordano,” Salita S. Lucia 5, I-98126 S. Lucia (Messina), Italy

Received 5 December 2006; revised 2 April 2007; accepted 2 April 2007

Available online 5 June 2007

Abstract

A novel synthesis route based on reverse co-precipitation under ultrasound irradiation has led to Cu–ZnO/ZrO₂ catalysts (Zn_{at}/Cu_{at}, 0–3; ZrO₂, 42–44 wt%) with a remarkable development of total surface area (S_{BET}, 120–180 m²/g) and very high dispersion (3–58%) and exposure (MSA 9–63 m²/g) of the active Cu phase. The activity pattern in the hydrogenation of CO₂ to CH₃OH (T_R, 433–533 K; P_R, 1.0–3.0 MPa) was addressed in comparison with a commercial Cu–ZnO/Al₂O₃ methanol synthesis catalyst. Volcano-shaped trends in total and metal surface area signal an optimum zinc loading (Zn/Cu, 0.3–0.7), ensuring higher concentration of active sites and methanol productivity values, whereas the basic relationships among dispersion, reducibility, and TOF indicate a structurally sensitive character of the title reaction and a superior reactivity of poorly dispersed Cu particles. Thermodynamic analysis of the reaction stream revealed that methanol formation proceeds along a parallel path, whereas a stronger “water affinity” accounts for the poorer performance of the conventional alumina-based catalyst compared with zirconia-based ones.

© 2007 Elsevier Inc. All rights reserved.

Keywords: Cu–ZnO/ZrO₂ catalysts; CO₂ hydrogenation; CH₃OH synthesis; Physicochemical characterization; Dispersion; Reducibility; Catalytic pattern; Structure sensitivity

1. Introduction

Incessant technological progress over the past century aimed at continuously improving lifestyle quality has produced a progressive deterioration of natural resources and rise in pollutant levels in the atmosphere, responsible for global warming (“greenhouse effect”) and, in turn, impressive climate changes in recent years [1,2]. Pressed by the imperative to avoid further irreversible damage to the environment with the resulting catastrophic consequences for the future of mankind, many countries worldwide are now pursuing a general reduction of pollutant and carbon dioxide emissions, the major contributors to the greenhouse effect [1]. Among the viable strategies to reduce carbon dioxide emissions, mostly “sequestration” and

novel process technologies based on “CO₂ recycling,” are actually attracting the major scientific and technological interest [3]. Indeed, the approach of using CO₂ as “reagent” for producing bulk chemicals like methanol and dimethylether (DME) [4–8] appears to be particularly attractive, because these are also potential substitutes for traditional oil-based fuels for automobiles, which may help reduce air pollution in metropolitan areas [4]. Accomplishing the strategic goal of reducing the Western nations’ dependence on oil, these energy carriers are in fact easily accessible from natural gas (NG) via syngas. The ability to exploit CO₂-rich NG resources and the possibility of decreasing the reforming temperature to reduce syngas generation costs [1–3] are other important advantages of the methanol synthesis via CO₂ hydrogenation.

Currently, methanol synthesis is run mostly on Cu–ZnO/Al₂O₃ catalysts at 493–573 K and a pressure of 5–10 MPa with a syngas feed containing typically 5% CO–5% CO₂ and H₂ [9–11]. However, recent studies have found that methanol

* Corresponding author. Fax: +39 090391518.

E-mail address: Francesco.Arena@unime.it (F. Arena).

Table 1
List of the studied catalysts and relative physicochemical properties

Code ^a	Chemical composition (%)			Zn _{at} /Cu _{at}	SABET (m ² /g _{cat})	PV (cm ³ /g _{cat})	APD (Å)	MSA ^b (m ² /g _{cat})	D _{Cu} ^b (%)	d _{Cu} ^b (nm)
	CuO	ZnO	ZrO ₂							
Cu(12)/ZrO ₂ (6)	58.6	0	41.4	0.0	118	0.33	74	8.7	3.3	32
Cu(11)ZnO(1)/ZrO ₂ (6)	51.9	4.6	43.5	0.1	128	0.24	91	17.4	6.2	17
Cu(10)ZnO(2)/ZrO ₂ (6)	45.0	11.8	43.2	0.3	163	0.59	118	63.0	27.6	4
Cu(9)ZnO(3)/ZrO ₂ (6)	41.2	14.8	44.0	0.4	174	0.56	106	60.8	29.1	4
Cu(8)ZnO(4)/ZrO ₂ (6)	36.2	19.6	44.2	0.5	162	0.54	110	59.7	32.5	3
Cu(7)ZnO(5)/ZrO ₂ (6)	31.6	24.0	44.4	0.7	159	0.36	85	59.3	37.0	3
Cu(3)ZnO(9)/ZrO ₂ (6)	15.1	41.8	43.1	2.7	147	0.35	73	44.7	57.9	2
ZnO(12)/ZrO ₂ (6)	0	56.1	43.9	–	103	0.31	121	–	–	–
Cu(4)ZnO(4)/Al ₂ O ₃ (6)	35.0	33.1	– ^c	0.9	105	0.23	70	34.4	19.2	5

^a Number in parentheses refer to the atomic/molecular concentration.

^b From “single-pulse” (363 K) N₂O titration measurements (see Ref. [60]).

^c Commercial synthesis catalyst containing Al₂O₃ (31.9 wt%) as carrier.

can be obtained with rates and carbon utilization factors superior than those of the traditional route by CO₂ hydrogenation [11,12]. Even if some details of the reaction mechanism remain controversial, several authors have in fact claimed that under typical industrial conditions, methanol is formed mostly via CO₂ hydrogenation, with CO serving as the CO₂ source and as a scavenger of oxygen atoms coming from water, which in turn acts as an inhibitor of the active metal sites [9–11]. Just water formation would account for the poorer performance of traditional alumina-supported catalysts in CO₂-rich syngas feedstocks [13–15] compared with zirconia-based systems [16–22]. Moreover, despite being generally attributed to a synergism of Cu⁰–Cu⁺ sites and the reactivity of ZnO-promoted catalysts [6,14,23–28], the catalytic role of Cu⁰ [29,30] and/or Cu–Zn alloy [31–37] also has been envisaged.

Many research groups have adopted unconventional preparation routes to improve the activity, selectivity, poison resistance, or lifetime of Cu–ZnO systems [20–24,26,38–53]. For example, Coteron and Hayhurst [54] found that Cu–Zn catalysts prepared by “spark-erosion” feature high methanol selectivity, whereas we ascribed higher TOF in the CO₂ hydrogenation reaction to a very “intimate” contact of the Cu/ZnO/ZrO₂ phases ensured by the “combustion” route [55]. Köppel et al. [22] and Sun and Sermon [56] adopted the sol–gel technique to enhance total and metal surface areas, whereas Jingfa et al. [57] emphasized the superior activity of oxalate-coprecipitated catalysts. Dopant addition [24,46–49] was found to improve either dispersion or Cu–Zn(O) contact area [20–22,26,38–45], whereas alternative active phases (e.g., Ag, Au) seem to exhibit superior selectivity in the CO₂ hydrogenation reaction [23,50–53].

Consequently, the present study was undertaken to assess the efficiency of a new preparation method based on reverse co-precipitation under ultrasound irradiation in improving the physicochemical properties of the Cu–ZnO/ZrO₂ system. Catalytic tests in a wide range of experimental conditions and the relative thermodynamic evaluations can provide fundamental insight into process optimization and structural factors controlling the functionality of the Cu–ZnO system in the CO₂ hydrogenation reaction.

2. Experimental

2.1. Materials

A series of Cu–ZnO/ZrO₂ catalysts with different Zn/Cu atomic ratios (0–3) and a constant zirconia loading (\approx 44 wt%) was prepared by the new reverse co-precipitation under ultrasound irradiation route [58] as follows. An aqueous solution (ca. 100 mL) of the Cu(NO₃)₂·3H₂O, Zn(NO₃)₂·6H₂O, and ZrO(NO₃)₂·nH₂O (Sigma Aldrich) precursors was added dropwise under vigorous stirring to a 0.1 M NaHCO₃ solution (500 mL) kept in an ultrasound bath (Bransonic B-120E1) operating at 47 kHz and with a power of 30 W ($T = 310$ – 320 K) [58]. The pH of the precipitating solution was maintained in the range of 7.0–7.5 by the continuous addition of a 0.1 M NaHCO₃ solution. After precipitation, the solid was kept for another 30 min under stirring and ultrasound irradiation, then aged at room temperature for 2 h, filtered, and washed with hot distilled water. Thereafter the catalysts were dried at 373 K for 16 h and further calcined in air at 623 K for 4 h. Powdered catalysts were pressed (40 MPa), crushed, and sieved to the particle size fraction (40–70 mesh) used for both characterization and testing measurements. A commercial Cu–ZnO/Al₂O₃ methanol synthesis catalyst (G66A, Sud Chemie AG) was used as a reference system. The catalysts’ relative notation and main physicochemical properties are listed in Table 1.

2.2. Physicochemical characterization

Surface area (S_{ABET}), pore volume (PV), and the pore size distribution (PSD) were determined from the nitrogen adsorption/desorption isotherms at 77 K, using a fully automated ASAP 2010 (Micromeritics) gas adsorption device. Before analysis, all the samples were outgassed at 423 K under vacuum for 2 h. The isotherms were elaborated according to the BET method for surface area calculation, with the Horwarth–Kavazoe and BJH methods used for micropore and mesopore evaluation, respectively.

Temperature-programmed reduction (TPR) measurements at 273–1073 K were performed in a continuous-flow apparatus

using a linear quartz microreactor (4 mm i.d.) fed with a 6% H₂/Ar mixture flowing at 60 stp mL/min and heated at the rate of 20 K/min. A ca. 15-mg catalyst sample was used, with H₂ consumption monitored by a TCD quantitatively calibrated with a commercial CuO standard (Carlo Erba) [59].

Metal surface area (MSA) values were obtained with $\pm 5\%$ accuracy by single-pulse (1.0 mL) N₂O titration ($T = 363$ K) [60]. Before measurements, catalysts were reduced in situ at 573 K in a H₂ flow (100 stp mL/min) for 1 h. After reduction, the samples were “flushed” in the He carrier flow at 583 K for 15 min, and then cooled to 363 K. For the MSA calculations, a Cu:N₂O = 2:1 chemisorption stoichiometry and a value of 1.46×10^{19} Cu atom/m² density were assumed, with the volume surface average particle size (d_{Cu}) obtained from the conventional formula

$$d_{Cu} \text{ (nm)} = \frac{104}{D \text{ (\%)}}$$

assuming a spherical shape of Cu particles [29,60].

X-ray diffraction (XRD) analysis of samples in the 2θ range 10–80° was performed using a Philips X-Pert diffractometer operating with Ni β -filtered CuK α radiation at 40 kV and 30 mA. Thermogravimetric (TG-DSC) analysis of the dried and calcined samples in the range 293–1073 K was performed using a Netzsch STA 409 C analyzer running at a heating rate of 12 K/min in air atmosphere.

2.3. Catalyst testing

Catalyst tests in the hydrogenation of CO₂ were performed at 433–533 K and 1.0–3.0 MPa using an Inconel microreactor (6 mm i.d.). A CO₂–H₂–N₂ reaction mixture with a molar ratio of 3/9/1 was fed at the rate of 40 stp mL/min (GHSV = 4400 N L/(h kg_{cat})) or 80 stp mL/min (GHSV = 8800 N L/(h kg_{cat})) on a 0.5-g catalyst sample diluted with 0.5 g of same-sized SiC. The temperature was controlled by a thermocouple in contact with the catalyst bed. Before each test, the catalysts were reduced in situ at 573 K for 1 h in H₂ flow (100 stp mL/min) at atmospheric pressure. Then the reactor was cooled to 433 K and the reaction mixture was admitted, raising the pressure to 1.0 or 3.0 MPa. The activity was probed by performing heating–cooling cycles to rule out “hysteresis” phenomena. The reaction stream was analyzed by a gas chromatograph equipped with a two-column analytical system connected to a flame ionization detector (CH₃OH, CH₃OCH₃) and thermal conductivity detector (CO, N₂, CO₂, H₂). Conversion values were calculated by both internal standard (a) and mass-balance (b) methods,

$$X_{CO_2} = 1 - \left[\left(\frac{CO_{2,out}}{CO_{2,in}} \right) \cdot \left(\frac{N_{2,in}}{N_{2,out}} \right) \right] \quad (a)$$

and

$$X_{CO_2} = \frac{CO_{2,out}}{\left(\sum_{prod} + CO_{2,out} \right)}, \quad (b)$$

with selectivity data obtained from standard formulas

$$S_{CH_3OH} = \frac{CH_3OH_{out}}{(1 - CO_{2,out})} \quad (a')$$

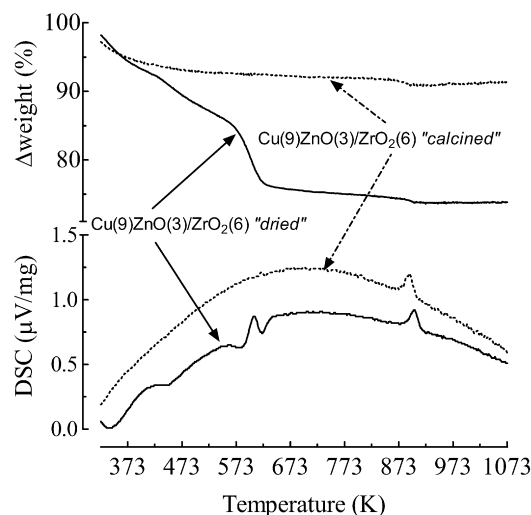


Fig. 1. TG and DSC profiles of the “dried” and “calcined” Cu(9)ZnO(3)/ZrO₂(6) catalyst.

and

$$S_{CH_3OH} = \frac{CH_3OH_{out}}{\sum_{prod}} \quad (b')$$

Each data set was obtained, with an accuracy of $\pm 3\%$, from an average of three independent measurements.

3. Results

3.1. Physicochemical characterization

The systematic TG-DSC study of representative “dried” and “calcined” catalyst samples was preliminarily carried out to determine the minimum calcination temperature for attaining complete decomposition of precursors. The TG-DSC pattern of the dried Cu(9)ZnO(3)/ZrO₂(6) catalyst (Fig. 1) exhibits considerable ($\approx 25\%$) weight loss in the range 300–620 K, with an exothermic peak at ca. 600 K and only negligible weight variations thereafter up to 1073 K. Indeed, with a ca. 5 wt% loss below 400 K due to dehydration, TGA confirms the substantial thermal stability of the catalyst sample previously calcined at 623 K for 4 h. Only a small exothermic peak at ca. 900 K, analogous to that observed for the dried sample, is associated with a comparably small weight loss ($< 1\%$). Based on this, we systematically adopted a calcination temperature of 623 K to ensure complete decomposition of catalyst precursor(s) and minimize sintering phenomena.

Surface characterization data confirm that the new synthesis route improves the total surface exposure to remarkably high levels (Table 1), although the ZnO content has a significant influence on catalyst texture (Fig. 2A). Lower S_{BET} (120–130 m²/g) values are in fact recorded at low (≤ 0.1) and high (> 0.7) Zn/Cu ratios, with the maximum value of 175 m²/g found for a Zn/Cu of 0.3–0.4 (Fig. 2A). It is noteworthy that similar changes in the Cu surface exposure account for a straight-line increase of MSA with S_{BET} from 9 to 63 m²/g_{cat} (Fig. 2B). Further, both pore volume (Fig. 2A) and

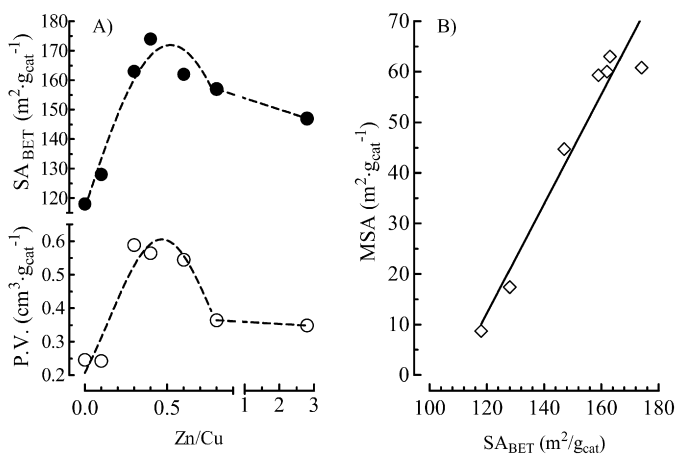


Fig. 2. (A) Effect of the Zn/Cu atomic ratio on the SA_{BET} and pore volume of the Cu–ZnO/ZrO₂ catalysts. (B) Relationship between MSA and SA_{BET} of the Cu–ZnO/ZrO₂ catalysts.

average pore diameter (Table 1) follow a trend analogous to that of SA_{BET} due to marked changes in the PSD (Fig. 3). The “unpromoted” Cu(12)/ZrO₂(6) system (Fig. 3A) displays a very “broad” and featureless PSD, accounting for a cumulative volume of ca. 0.33 cm³/g. In contrast, the catalyst with intermediate Zn/Cu ratio (0.4) is characterized by a prevalence of 70–120 Å mesopores (Fig. 3B), resulting in a much greater cumulative volume (ca. 0.6 cm³/g). Although a pronounced maximum is centered at 90 Å (Fig. 3C), the Cu(3)ZnO(9)/ZrO₂(6) sample with the largest (2.7) Zn/Cu ratio has a pore volume (0.3 cm³/g) comparable with that of low Zn-loaded samples (Table 1).

The results of XRD measurements performed to obtain information on the crystalline phases present both on dried (Fig. 4A) and calcined (Fig. 4B) catalysts are collected in Fig. 4. Apart from minor differences in the 2θ range of 15–30°, the rather featureless diffraction patterns indicate a significant lack of “long-range” crystalline order in both dried and calcined Cu(9)ZnO(3)/ZrO₂(6) samples (Fig. 4A). However, similar diffraction patterns signal that all of the calcined samples (Fig. 4B) with Zn/Cu > 0.1 are characterized by a prevalently amorphous architecture. Only at low (≤0.1) Zn loading are the typical reflexes of a crystalline tenorite (JCPDS 5-661) CuO phase evident [59]. Applying Sherrer’s equation to the (002) line produces mean CuO particle sizes of 12 nm for Cu(12)/ZrO₂(6) and 10 nm for Cu(11)ZnO(1)/ZrO₂(6). Then the significantly larger *d*_{Cu} value quoted for the former system from N₂O uptake measurements (Table 1) should indicate a major resistance to sintering of the promoted Cu(11)ZnO(1)/ZrO₂(6) sample.

TPR measurements were carried out to highlight the reduction pattern of the various catalysts and settle a proper activation (reduction) protocol for testing. The reduction profiles of the studied catalysts are shown in Fig. 5, and the onset (*T*_{0,red}) and maximum (*T*_{Mi}) temperatures and the values of hydrogen consumption are summarized in Table 2. All of the systems display reduction profiles characterized by a main peak with a *T*_{M1} maximum between 486 and 511 K, well below that of the standard bulk CuO (ca. 570 K), accounting for a regu-

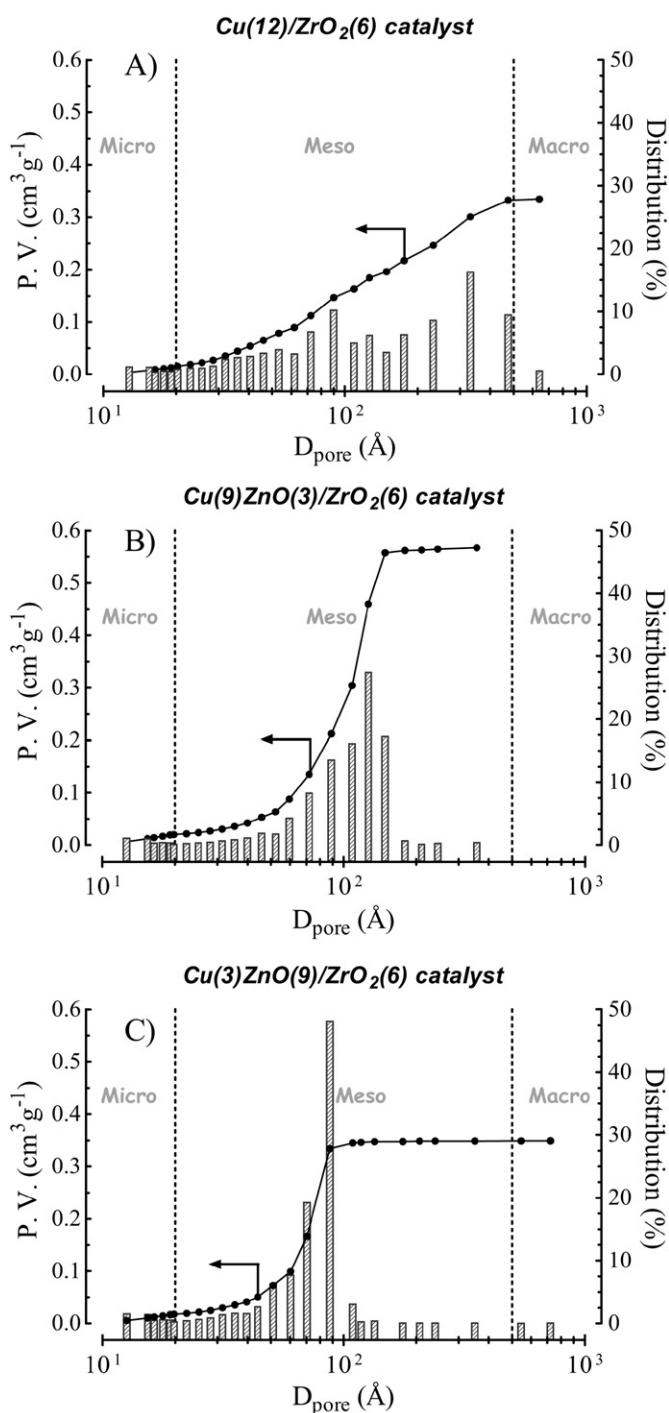


Fig. 3. Pore size distribution curves of representative Cu–ZnO/ZrO₂ catalysts.

lar rise in the onset temperature of reduction with the Zn/Cu ratio (Table 2). A shoulder on the left side of the maximum is particularly evident at low Zn content [Cu(12)/ZrO₂(6) and Cu(11)ZnO(1)/ZrO₂(6)], whereas the peak is sharper and much more symmetrical for all of the other systems. The amount of hydrogen consumption at 273–573 K is always close to (although somewhat greater than) the stoichiometric amount for CuO reduction ($H_2/Cu = 1.05\text{--}1.22$). Moreover, a baseline drift at 573–1073 K with a poorly resolved *T*_{M2} maximum (830–890 K), the shape of which depends on the zinc loading,

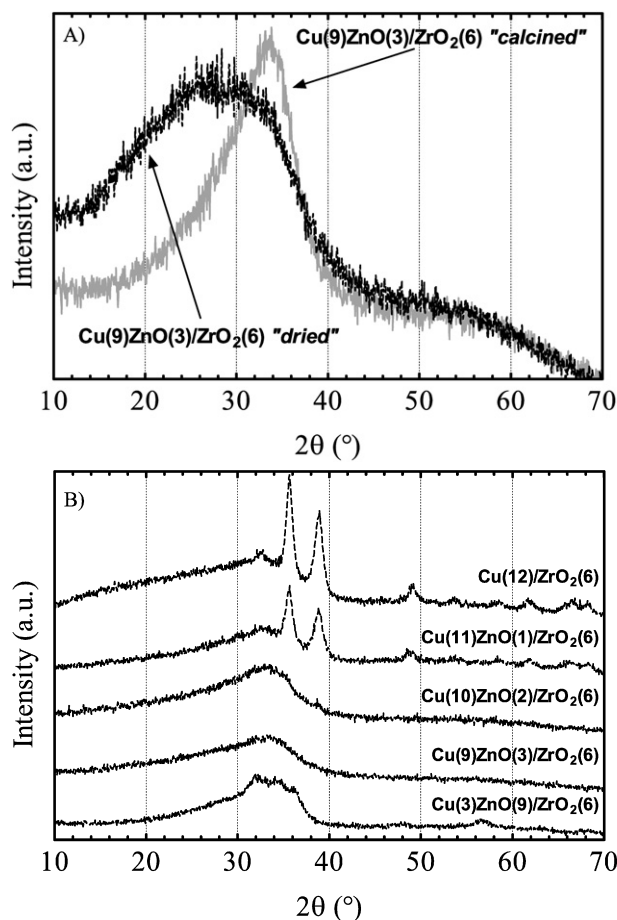


Fig. 4. XRD patterns of the “dried” and “calcined” Cu(9)ZnO(3)/ZrO₂(6) samples (A) and of the calcined catalysts with different Zn/Cu ratio (B).

Table 2

TPR data of Cu–ZnO/ZrO₂ catalysts. Onset temperature of reduction ($T_{o,red}$), temperature of peak maxima (T_{M_i}) and extent of hydrogen consumption

Catalyst	$T_{o,red}$ (K)	T_{M1} (K)	T_{M2} (K)	mmol H ₂ tot/g _{cat}	H ₂ /Cu ^a
Cu(12)/ZrO ₂ (6)	388	501	831	9.2	1.22
Cu(11)ZnO(1)/ZrO ₂ (6)	390	511	870	7.8	1.15
Cu(10)ZnO(2)/ZrO ₂ (6)	395	486	831	8.4	1.06
Cu(9)ZnO(3)/ZrO ₂ (6)	404	488	845	8.2	1.13
Cu(8)ZnO(4)/ZrO ₂ (6)	428	497	826	6.7	1.05
Cu(7)ZnO(5)/ZrO ₂ (6)	431	501	845	6.1	1.07
Cu(3)ZnO(9)/ZrO ₂ (6)	448	506	862	2.7	1.11
ZnO(12)/ZrO ₂ (6)	–	–	891	1.4	–
Cu(4)ZnO(4)/Al ₂ O ₃ (6)	422	521	962	6.1	0.98
CuO “bulk”	474	568	–	12.6	1.00

^a In the T range: 273–573 K.

Table 3

Conversion–selectivity data (X_{CO_2} – S_{CH_3OH}) of Cu–ZnO/ZrO₂ and reference catalysts in the CO₂ hydrogenation reaction at different temperature and pressure (GHSV, 4400 N L/(hkg_{cat}))

Catalyst	P_R , 1.0 MPa			P_R , 3.0 MPa		
	T_R , 473 K	T_R , 493 K	T_R , 513 K	T_R , 473 K	T_R , 493 K	T_R , 513 K
Cu(12)/ZrO ₂ (6)	3.9–63.0	7.1–41.1	11.4–25.2	7.2–70.2	12.6–57.4	17.6–48.8
Cu(10)ZnO(2)/ZrO ₂ (6)	5.8–55.2	10.0–35.5	14.1–18.0	6.2–66.9	10.8–49.9	16.5–45.0
Cu(3)ZnO(9)/ZrO ₂ (6)	4.1–59.5	8.6–34.6	13.3–16.9	6.5–70.9	12.6–55.2	17.5–48.4
Cu(4)ZnO(4)/Al ₂ O ₃ (6)	5.5–53.8	10.2–30.9	14.2–18.6	6.4–72.0	11.5–56.0	15.9–48.4

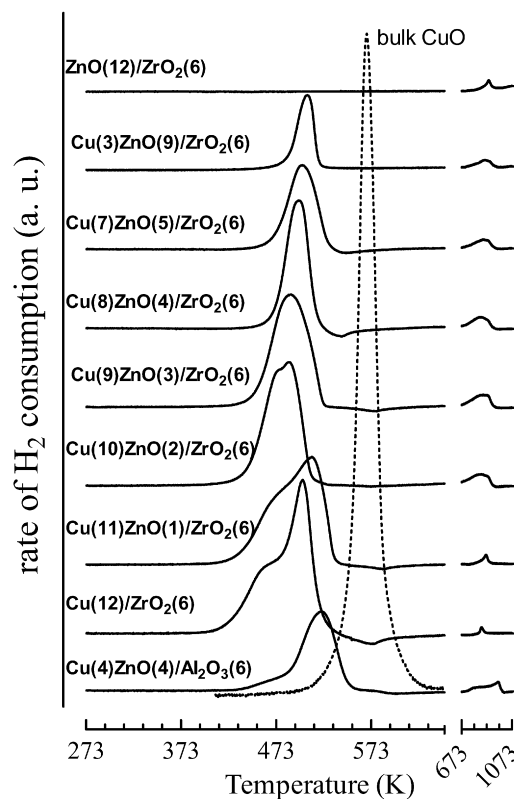


Fig. 5. TPR profiles of the Cu–ZnO/ZrO₂ and reference catalysts.

is associated with an ongoing reduction of the ZnO promoter and/or the decomposition of a residual carbonate phase (Fig. 1).

The TPR profile of the reference catalyst is similar to that of Cu–ZnO/ZrO₂ catalysts, with a main peak centered at 521 K and markedly skewed on the low- T side ($T_{o,red} = 422$ K), accounting for a stoichiometric H₂/Cu ratio (Table 2). Also at $T > 573$ K, the trend in H₂ consumption appears similar, even though a poorly resolved maximum occurs at temperatures above those for Cu–ZnO/ZrO₂ catalysts (Table 2).

3.2. Catalytic activity

Activity data of representative catalysts in the CO₂ hydrogenation reaction ($T_R = 473$ –513 K; GHSV = 4400 N L/(hkg_{cat}); $P_R = 1.0$; 3.0 MPa) are collected in Table 3 in terms of CO₂ conversion (X_{CO_2}) and CH₃OH selectivity (S_{CH_3OH}). At lower pressure, all the systems feature a similar catalytic pattern characterized by X_{CO_2} values rising from 4 to 14%, counterbalanced by a drop in S_{CH_3OH} from 63 to 17%, whereas

at 3.0 MPa, a systematic increase of X_{CO_2} from 6 to 18% implies a much smaller decrease in $S_{\text{CH}_3\text{OH}}$ from 73 to 45%. Overall, under such experimental conditions, a very slight affect of the composition on reactivity of the Cu–ZnO system is found. However, comparing the selectivity–conversion pattern of the Cu(10)ZnO(2)/ZrO₂(6) and reference catalyst at higher GHSV (8800 N L/(h kg_{cat})) demonstrates the poorer performance of the latter system at both 1.0 and 3.0 MPa, mainly in terms of methanol selectivity (Fig. 6). Through a systematic decrease with conversion, at 1.0 MPa an increase in X_{CO_2} from 0.5 to 2.5% (reference catalyst) and to 3.5% [Cu(10)ZnO(2)/ZrO₂(6)] causes a steep decay in $S_{\text{CH}_3\text{OH}}$, from 100% to ca. 65%. At 3.0 MPa, a much more pronounced increase in X_{CO_2} (from ca. 2.5% to 7–7.5%) accounts for “smoother” decreases in the $S_{\text{CH}_3\text{OH}}$ from 100 to 50% on the reference catalyst and 75% on Cu(10)ZnO(2)/ZrO₂(6). Accordingly, productivity data (STY, kg_{CH₃OH}/(kg_{cat} h)) as a function of the Zn/Cu ratio (Fig. 7) display an optimum Zn/Cu ratio of 0.3–0.5, ensuring higher STY values at both low (Fig. 7A) and higher (Fig. 7B) GHSV's. In

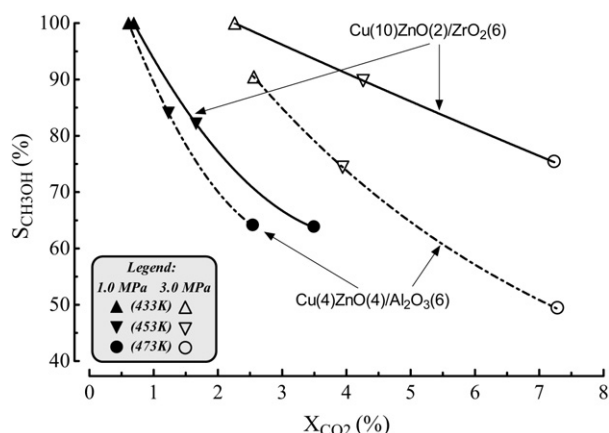


Fig. 6. Selectivity to methanol vs X_{CO_2} (GHSV, 8800 N L/(h kg_{cat})) for the Cu(10)ZnO(2)/ZrO₂(6) and reference catalysts at 1.0 and 3.0 MPa in the range 473–513 K.

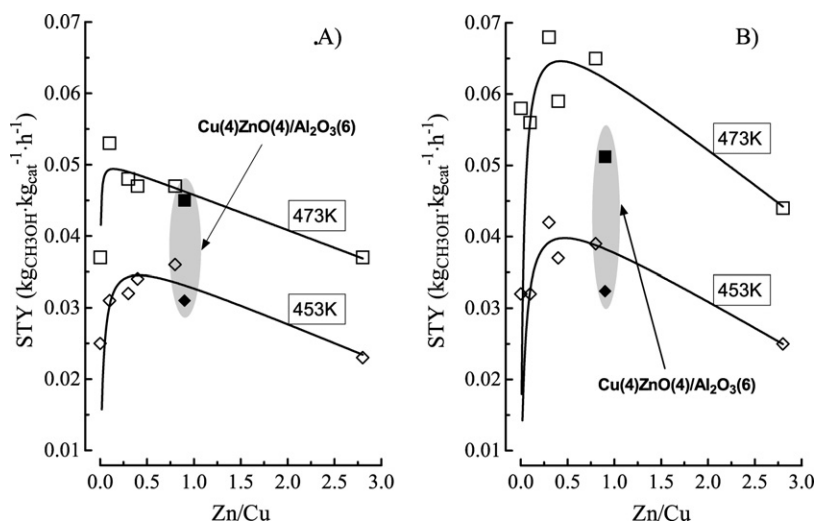


Fig. 7. STY of Cu–ZnO/ZrO₂ catalysts vs Zn/Cu ratio at 453 and 473 K and 1.0 MPa. (A) GHSV, 4400 N L/(h kg_{cat}); (B) GHSV, 8800 N L/(h kg_{cat}).

comparison, the productivity of the reference system is particularly depressed at the highest GHSV (Fig. 7B).

Short-term stability tests on the reference and Cu(9)ZnO(3)/ZrO₂(6) catalysts at 473 K and 1.0 MPa (GHSV = 4400 N L/(h kg_{cat})) were carried out to address the occurrence of potential deactivation phenomena. Both catalysts exhibited constant conversion–selectivity values during 18 h of time on stream, indicating substantial stability of the Cu–ZnO system irrespective of the carrier.

4. Discussion

4.1. Aims and strategy of the design of the new synthesis route

Addressing the effects of the preparation method (e.g., combustion, coprecipitation), we previously ascertained a marked influence of the textural properties on the CO₂ hydrogenation pattern of Cu–ZnO/ZrO₂ catalysts [55]. However, the low development of total and/or metal surface areas has prompted the search for more effective synthesis routes to improve the texture and reactivity of the Cu–ZnO/ZrO₂ system [55]. Due to the different precipitation kinetics of each cation, the conventional coprecipitation technique leads to mixtures of more or less small “monophase” particles, with limited dispersion of the active phase in the final catalyst [22,40,55–57,61]. To overcome this drawback, we attempted to accomplish simultaneous precipitation of the three cations (Cu²⁺, Zn²⁺, and ZrO²⁺) through a slow dropwise addition of the precursor solution to a large volume of the precipitating agent (i.e., reverse coprecipitation), keeping the pH between 7.0 and 7.5 to allow for coprecipitation of precursors mostly as (hydroxi)carbonates. Moreover, evaluating the influence of the ultrasound field on the textural properties of the representative Cu(9)ZnO(3)/ZrO₂(6) system, we preliminarily found improvements in both S_{ABET} (≈10%) and MSA (≈20%) due to irradiation during co-precipitation [55,58]. Based on such evidence, we systematically adopted the reverse co-precipitation under ultrasound irradiation technique for catalyst preparation.

4.2. Structural properties

Surface area and, mostly, metal dispersion and MSA values (Table 1) were much larger than those reported so far for bulky Cu-based catalysts [22,40,55–57,61]. This finding provides the best indication of the successful strategy of design of the reverse co-precipitation under ultrasound irradiation route [58]. Indeed, the improvement in textural properties depends on the characteristics of the preparation method that allows precipitation of very small oxide particles, also ensuring very good mixing of the various precursors in the first stage of solid formation [58]. Together, the evident CO₂ release during aging, the weight loss (Fig. 1) corresponding to ca. 70% decomposition of carbonates, and the peculiar diffraction pattern of the dried Cu(9)ZnO(3)/ZrO₂(6) sample (Fig. 4A) provide probatory experimental evidence supporting the formation of a homogeneous hydroxycarbonate phase in the co-precipitation stage. Its subsequent decomposition by the “soft” calcination treatment (at 623 K) retains a disordered architecture with no significant long-range crystalline order (Fig. 4B). Meanwhile, the very fine texture of the oxide particles, the sintering of which would be hindered by the release of great amounts of CO₂ from (hydroxy)carbonate decomposition, accounts for a very significant surface exposure. Then the stabilization of a prevalently amorphous structure for Zn/Cu > 0.1 (Fig. 4) matches the greater development of total and metal surface area (Fig. 2). Whereas at low ZnO concentration (Zn/Cu < 0.3), segregation of the crystalline CuO (tenorite) phase (Fig. 4) matches the lower SA_{BET}, MSA, and *D* values of the Cu(12)/ZrO₂(6) and Cu(11)ZnO(1)/ZrO₂(6) samples (Table 1). Therefore, the shape of the reduction peak (Fig. 5) also should be related to the morphology of the CuO phase, which is in turn affected by the ZnO loading. In fact, a broad and “stepped” TPR peak could signal the reduction of different-sized CuO particles in the Cu(12)/ZrO₂(6) and Cu(11)ZnO(1)/ZrO₂(6) samples. Considering surface (Table 1) and structural (Fig. 4) characterization data, and the higher *T*_{M1} value recorded for the bulk CuO system (Table 2), the component at higher temperature (Fig. 5)

can be assigned to the more difficult reduction of larger crystalline CuO particles [59,61]. In contrast, a narrower and more symmetric peak shape of the catalysts with Zn/Cu > 0.1 denotes the simultaneous reduction of smaller CuO particles with a much more uniform size distribution [59,61]. Such data infer a fundamental role of the ZnO as a structural promoter of the active Cu phase, which in turn affects the reducibility of the system. In fact, an exponential increase in metal dispersion with the Zn/Cu ratio (Fig. 8A) parallels a straightforward increase in *T*_{o,red} with ZnO loading (Fig. 8B). This suggests that a weaker Cu–O bond strength enables easier generation of “nucleation” metal centers (e.g., *T*_{o,red}) on large CuO particles characterized by only slight (if any) interaction with the ZnO promoter, whereas the higher dispersion and stronger promoter interaction of the CuO phase cause a shift of *T*_{o,red} to higher temperatures at greater ZnO loadings. Nevertheless, a faster reduction of smaller CuO particles in the bulk would explain the lower *T*_{M1} values of the systems characterized by larger Zn/Cu ratios [61]. Overall, higher *T*_{M1} and *T*_{M2} values signal a more difficult reduction of both active phase and promoter on the reference system, likely due to the stronger interaction with the Al₂O₃ carrier [61]. Spanning a dispersion range (3–58%) much larger than that attained so far for massive Cu-based catalysts [22,40,55–57,61], the novel synthesis route indicates a very effective CuO–ZnO/ZrO₂ interaction affecting the texture, morphology, and reactivity of Cu–ZnO/ZrO₂ catalysts [61].

4.3. Structure–activity relationships

Although different physicochemical properties point to an optimum Zn/Cu ratio ensuring the maximum development of SA_{BET} and MSA (Fig. 2), catalyst productivity is not a direct function of such parameters [31,61,62]. Actually, variations in MSA of about 1 order of magnitude (9–63 m²/g) reflect in a less than threefold rise in STY between minimum and maximum (Fig. 7). Then it can be argued that the different reactivities of active centers, a multicenter reaction path, and/or thermodynamic factors combine to “smooth” the potential of the

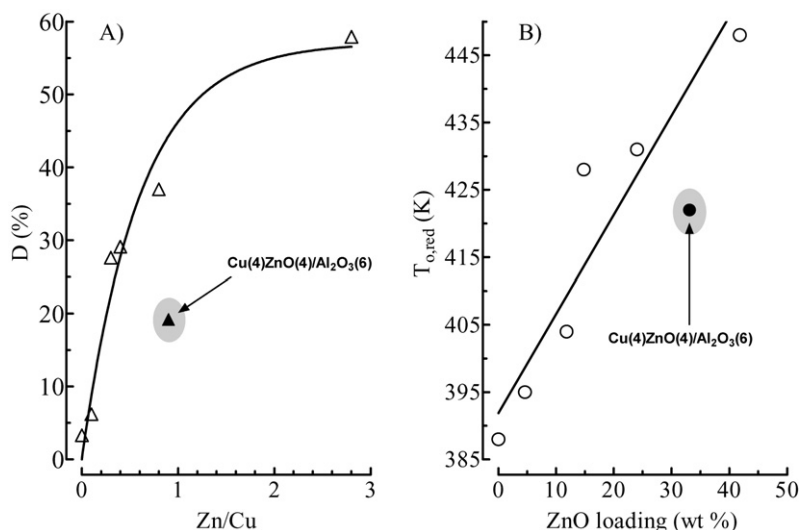


Fig. 8. (A) Effect of the Zn/Cu ratio on metal dispersion; (B) relationship between onset temperature of reduction (Table 2) and ZnO loading.

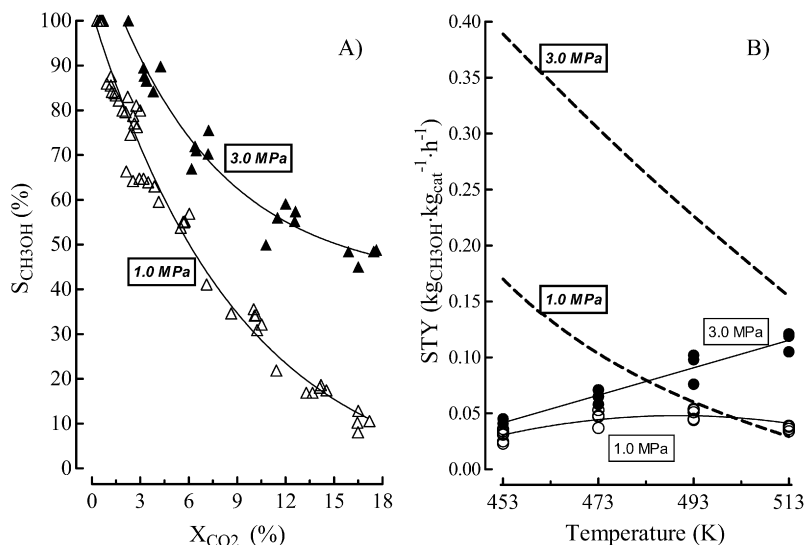


Fig. 9. (A) Methanol selectivity vs conversion data of the various catalysts in the range 453–513 K at 1.0 and 3.0 MPa. (B) STY of the various catalysts in the range 453–513 K. (---) Represent equilibrium data at 1.0 and 3.0 MPa.

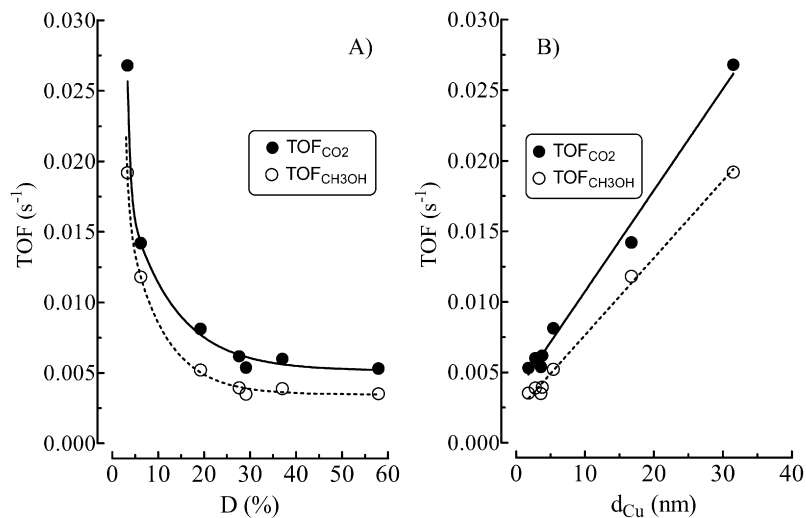


Fig. 10. Influence of the metal dispersion (A) and average Cu particle diameter (B) on the turnover frequency of CO_2 conversion and CH_3OH formation (T_{R} , 473 K; P_{R} , 1.0 MPa; GHSV, $8800 \text{ N L}/(\text{h kg}_{\text{cat}})$).

MSA exposure. This is confirmed by the fact that the catalytic pattern of all Cu–ZnO/ZrO₂ catalysts can be described by general relationships between selectivity and conversion (Fig. 9A) and between STY and temperature (Fig. 9B). Due to the marked volume decrease of the synthesis reaction, these correlations are strongly dependent on pressure. Overall, a much smaller decrease in methanol selectivity coupled with higher conversions provide substantially larger STY values at 3.0 MPa (Fig. 9B), with the maximum values (0.12–0.14 $\text{kg}_{\text{CH}_3\text{OH}}/(\text{kg}_{\text{cat}} \text{h})$) equal to or greater than those attained so far under even more favorable reaction conditions [22,29,35,41].

To highlight the slight influence of MSA on STY, it is helpful to evaluate the influence of Cu dispersion on the reactivity of the metal phase. The turnover frequency (TOF, s^{-1}) of CH_3OH formation and CO_2 conversion ($T_{\text{R}} = 473 \text{ K}$; $P_{\text{R}} = 1.0 \text{ MPa}$; GHSV = $8800 \text{ N L}/(\text{h kg}_{\text{cat}})$) as functions of Cu dispersion (Fig. 10A) and particle size (Fig. 10B) are shown in Fig. 10.

Matching with the TOF values of methanol reforming reactions under similar experimental conditions [61], such values depict analogously decreasing curves (Fig. 10A), accounting for the linear decrease in reactivity of metal sites with d_{Cu} (Fig. 10B). Considering the close relationship between particle size and particle morphology, the latter trend may indicate a different functionality of Cu sites located at different positions of the crystal structure, roughly mirroring the density of planar sites with relative particle sizes [23,32,33,61]. However, according to the direct relationship between $T_{\text{O,red}}$ and ZnO loading (Fig. 8B), a modification in the electronic properties of smaller Cu particles could also produce a stronger bonding of oxygen-containing intermediates (e.g., formate, water, hydroxyls), resulting in low TOF values [23,32,33,61,63]. The possibility that high ZnO loadings can depress the stabilization of Cu^+ sites in the octahedral cavities of the zirconia carrier [6], perhaps due to a stronger CuO–ZnO interaction, must

Table 4
List of reactions considered for thermodynamic evaluations of catalytic activity data

Reaction	Stoichiometry	K_p^a				
		453 K	473 K	493 K	513 K	533 K
1	$\text{CO}_2 + 3\text{H}_2 \rightleftharpoons \text{CH}_3\text{OH} + \text{H}_2\text{O}$	1.81E-4	9.60E-5	5.33E-5	3.08E-5	1.84E-5
2	$\text{CO}_2 + \text{H}_2 \rightleftharpoons \text{CO} + \text{H}_2\text{O}$	2.72E-3	4.26E-3	6.44E-3	9.41E-3	1.33E-2
3	$\text{CH}_3\text{OH} \rightleftharpoons \text{CO} + 2\text{H}_2$	1.50E+1	4.44E+1	1.21E+2	3.05E+2	7.25E+2

^a Equilibrium pressure constant referred to pressure expressed in MPa.

be considered. This could enhance the negative effect of dispersion (>10%) on TOF in the case of a “multisite” reaction path involving Cu^0 and Cu^+ centers for hydrogen and CO_x adsorption/activation [6,14,23–28,40,55]. In the case of a reaction path involving the adsorption/activation of CO_2 on zirconia carrier [64], progressively increased coverage of the ZrO_2 surface by ZnO could occur to depress the TOF at high Zn/Cu ratios.

4.4. Thermodynamic analysis

A thermodynamic analysis of the reaction stream [65] was carried out to address the kinetics of the various functionalities and the influence of thermodynamics thereon. In particular, CO_2 hydrogenation can be described by a reaction network involving (1) the synthesis of methanol, (2) the reverse water–gas shift (RWGS), and (3) the methanol decomposition equilibriums:



and



Here (3) represents a linear combination of (1) and (2), and thus the thermodynamic evaluation depends on the analysis of (1) and (2), although the (3) can shed light on the $\text{CO}/\text{CH}_3\text{OH}$ distribution [e.g., $K_3 = \{[(P_{\text{CO}}) \times (P_{\text{H}_2})^2]/(P_{\text{CH}_3\text{OH}})]\}$. Substituting the P_x values (from conversion–selectivity data) into the expression of the equilibrium constants, we obtained experimental K_{exp} values for the above reactions. Then the ratio (β) between K_{exp} and the corresponding value of the equilibrium constant K_{eq} (Table 4) represents the distance from equilibrium as a measure of the relative kinetics of forward and reverse functionalities. The values of the various β_x at various temperatures at 1.0 (A) and 3.0 MPa (B) are shown in Fig. 11. Such data confirm that at the highest GHSV, all reactions below 473 K proceed under a prevailing kinetic regime. Moreover, although the trend of increasing β_1 and β_2 indicates a parallel reaction network, a steeper increase in β_1 leads to a steady decrease in β_3 at all pressures; that is, a β_3 value larger than that recorded at higher pressure (Fig. 11B) indicates that the Cu-ZnO/ZrO_2 system has a specific functionality for the hydrogenation of CO_2 (reaction (1)) rather than that of CO (reaction (3)). But although β_2 values are affected only slightly (if at all) by a rise in pressure (according to the negligible volume variation of the RWGS reaction), the lower β_1 values at 3.0 MPa indicate a decrease in the relative rate of methanol formation. This finding proves

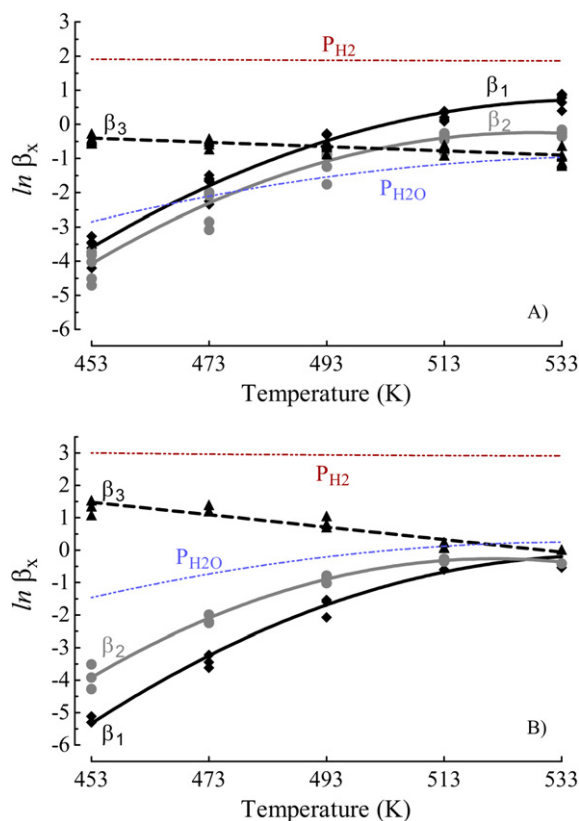


Fig. 11. Thermodynamic analysis of the reaction stream. Effect of temperature on the β_x values (e.g., $\beta = K_{\text{exp}}/K_{\text{eq}}$) of the reactions listed in Table 4 at 1.0 (A) and 3.0 MPa (B). For reference, the average experimental values of water vapor and hydrogen pressure are also shown.

that the rate of the synthesis reaction does not increase with the potential of the gas phase, due to the lower dependence of reaction kinetics on pressure. This is in agreement with the fact that the RDS is the surface decomposition of the formate intermediate and/or the abstraction of oxygen derived from its decomposition [23,33,63]. Accordingly, the RDS would proceed at a lower rate at higher surface coverage (higher P_R) and on low-index sites of small Cu particles [23,32,33,63]. Moreover, such data also demonstrate the “negative” role of water [see reactions (1) and (2)] on the methanol synthesis rate. Favoring water desorption, a temperature increase and/or pressure decrease mainly enhance(s) the rate of CH_3OH formation, despite the rise in $P_{\text{H}_2\text{O}}$ (Fig. 11). Then a much stronger chemical affinity of alumina carrier for water, enabling more extensive wetting of the catalyst surface, should account for the poorer performance of the reference $\text{Cu}(4)\text{Zn}(4)/\text{Al}_2\text{O}_3(6)$ catalyst in the title reaction (Figs. 6 and 7).

5. Conclusions

The activity-selectivity pattern of the Cu–ZnO/ZrO₂ system in the hydrogenation of CO₂ to methanol has been explored, with evaluation of kinetic and thermodynamic factors affecting catalytic functionality. The main findings of this work can be summarized as follows:

- A new method for preparing Cu–ZnO/ZrO₂ catalysts, based on reverse coprecipitation under ultrasound irradiation, provides a significant improvement in the total surface exposure as well as in the dispersion and surface area of the active metal phase.
- Basic relationships among surface area, dispersion, and catalyst reducibility point to a strong promoting effect of ZnO on catalyst texture.
- Marked changes in TOF with metal dispersion indicate the structurally sensitive character of the title reaction.
- Thermodynamic analysis of the reaction stream demonstrates the prevailing functionality of the title system for methanol formation via CO₂ hydrogenation.
- The negative effect of water on the rate of methanol formation accounts for the poorer catalytic performance of the reference Cu–ZnO/Al₂O₃ catalyst in the title reaction.

References

- [1] G.A. Olah, A. Goepfert, G.K. Surya Prakash, in: *Beyond Oil and Gas: The Methanol Economy*, Wiley–VCH, Weinheim, 2006.
- [2] G.A. Olah, A. Goepfert, G.K. Surya Prakash, *Catal. Lett.* 93 (2004) 1.
- [3] C. Song, *Catal. Today* 115 (2006) 2.
- [4] R.H. Borgwardt, *Ind. Eng. Chem. Res.* 37 (1998) 3760.
- [5] D. Mao, W. Yang, J. Xia, B. Zhang, Q. Song, Q. Chen, *J. Catal.* 230 (2005) 140.
- [6] K. Sun, W. Lu, F. Qiu, S. Liu, X. Xu, *Appl. Catal. A* 252 (2003) 243.
- [7] J. Xia, D. Mao, B. Zhang, Q. Chen, Y. Tang, *Catal. Lett.* 98 (2004) 235.
- [8] J.H. Kim, M.J. Park, S.J. Kim, O.S. Joo, K.D. Jung, *Appl. Catal. A* 264 (2004) 37.
- [9] G.C. Chinchen, P.J. Denny, J.R. Jennings, M.S. Spencer, K.C. Waugh, *Appl. Catal.* 36 (1988) 1.
- [10] G.C. Chinchen, K. Mansfield, M.S. Spencer, *Chemtech* 11 (1990) 692.
- [11] J.C.J. Bart, R.P.A. Sneeden, *Catal. Today* 2 (1987) 1.
- [12] G. Jia, Y. Tan, Y. Han, *Ind. Eng. Chem. Res.* 45 (2006) 1152.
- [13] M. Saito, T. Fujitani, M. Takeuchi, T. Watanabe, *Appl. Catal. A* 138 (1996) 311.
- [14] T. Inui, H. Hara, T. Takeguchi, J.B. Kim, *Catal. Today* 36 (1997) 25.
- [15] S. Fujita, M. Usui, H. Ito, N. Takezawa, *J. Catal.* 157 (1995) 403.
- [16] B. Denise, R.P.A. Sneeden, *Appl. Catal.* 28 (1986) 235.
- [17] Y. Amenomiya, *Appl. Catal.* 30 (1987) 57.
- [18] D. Gasser, A. Baiker, *Appl. Catal.* 48 (1989) 279.
- [19] A. Baiker, M. Kilo, M. Maciejewski, S. Menziand, A. Wokaun, *Stud. Surf. Sci. Catal.* 75 (1993) 1257.
- [20] C. Frohlich, R.A. Köppel, A. Baiker, M. Kilo, A. Wokaun, *Appl. Catal. A* 103 (1993) 275.
- [21] J. Słoczynski, R. Grabowski, A. Kozłowska, P. Olszewski, M. Lachowska, J. Skrzypek, J. Stock, *Appl. Catal. A* 249 (2003) 129.
- [22] R.A. Köppel, C. Stöcker, A. Baiker, *J. Catal.* 179 (1998) 515.
- [23] J. Yoshihara, C.T. Campbell, *J. Catal.* 161 (1996) 776.
- [24] G.C. Chinchen, K.C. Waugh, D.A. Whan, *Appl. Catal.* 25 (1986) 101.
- [25] K. Klier, *Adv. Catal.* 31 (1982) 243.
- [26] J. Toyir, P.R. de la Piscina, J.L.G. Fierro, N. Homs, *Appl. Catal. B* 29 (2001) 207.
- [27] S. Imo, J. Wu, J. Toyir, M. Saito, M. Takeuchi, T. Watanabe, *Stud. Surf. Sci. Catal.* 114 (1998) 549.
- [28] H.Y. Chen, L. Chen, J. Lin, K.L. Tan, J. Li, *J. Phys. Chem. B* 102 (1998) 1994.
- [29] J. Słoczynski, R. Grabowski, A. Kozłowska, P. Olszewski, J. Stock, J. Skrzypek, M. Lachowska, *Appl. Catal. A* 278 (2004) 11.
- [30] J. Toyir, P.R. de la Piscina, J. Llorca, J.L.G. Fierro, N. Homs, *Phys. Chem. Chem. Phys.* 3 (2001) 4837.
- [31] T. Fujitani, J. Nakamura, *Catal. Lett.* 56 (1998) 119.
- [32] P.L. Hansen, J.B. Wagner, S. Helveg, J.R. Rosrup-Nielsen, B.S. Clausen, H. Topsøe, *Science* 295 (2002) 2053.
- [33] C.V. Ovesen, B.S. Clausen, J. Schiøtz, P. Stoltze, H. Topsøe, J.K. Nørskov, *J. Catal.* 168 (1997) 133.
- [34] I. Nakamura, T. Uchijima, J. Nakamura, T. Fujitani, *Surf. Sci.* 383 (1997) 285.
- [35] Y. Choi, K. Futagami, T. Fujitani, J. Nakamura, *Catal. Lett.* 73 (2001) 27.
- [36] T. Fujitani, J. Nakamura, *Appl. Catal. A* 191 (2000) 111.
- [37] Y. Choi, K. Futagami, T. Fujitani, J. Nakamura, *Appl. Catal. A* 208 (2001) 163.
- [38] K. Omata, Y. Watanabe, T. Umegaki, G. Ishiguro, M. Yamada, *Fuel* 81 (2002) 1605.
- [39] H.Y. Chen, S.P. Lau, L. Chen, J. Lin, C.H.A. Huan, K.L. Tan, J.S. Pan, *Appl. Surf. Sci.* 152 (1999) 193.
- [40] J. Wambach, A. Baiker, A. Wokaun, *Phys. Chem. Chem. Phys.* 1 (1999) 5071.
- [41] C. Yang, Z. Ma, N. Zhao, W. Wei, T. Hu, Y. Sun, *Catal. Today* 115 (2006) 222.
- [42] R.A. Köppel, A. Baiker, A. Wokaun, *Appl. Catal.* 84 (1992) 77.
- [43] R.A. Köppel, A. Baiker, C. Schild, A. Wokaun, *Stud. Surf. Sci. Catal.* 69 (1991) 59.
- [44] Y. Nitta, T. Fujimatsu, Y. Okamoto, T. Imanaka, *Catal. Lett.* 17 (1993) 157.
- [45] N. Kanoun, M.P. Astier, G.M. Pajonk, *Catal. Lett.* 15 (1992) 231.
- [46] L. Znak, K. Stolecki, J. Zielirski, *Catal. Today* 101 (2005) 65.
- [47] K. Pokrovski, M.D. Rhodes, A.T. Bell, *J. Catal.* 235 (2005) 368.
- [48] I. Melián-Cabrera, M.L. Granados, J.L.G. Fierro, *J. Catal.* 210 (2002) 285.
- [49] L. Ma, T. Tran, M.S. Wainwright, *Top. Catal.* 22 (2003) 295.
- [50] S.E. Collins, D.L. Chivassa, A.L. Bonivardi, M.A. Baltanás, *Catal. Lett.* 103 (2005) 83.
- [51] W.J. Shen, A. Kobayashi, Y. Ichihashi, Y. Matsumura, M. Haruta, *Catal. Lett.* 73 (2001) 161.
- [52] W.J. Shen, Y. Ichihashi, Y. Matsumura, *Catal. Lett.* 79 (2002) 125.
- [53] W.J. Shen, Y. Ichihashi, H. Ando, Y. Matsumura, M. Okumura, M. Haruta, *Appl. Catal. A* 217 (2001) 231.
- [54] A. Coteron, A.N. Hayhurst, *Appl. Catal. A* 101 (1993) 151.
- [55] F. Arena, L. Spadaro, O. Di Blasi, G. Bonura, F. Frusteri, *Stud. Surf. Sci. Catal.* 147 (2004) 385.
- [56] Y. Sun, P.A. Sermon, *Catal. Lett.* 29 (1994) 361.
- [57] D. Jingfa, S. Qi, Z. Yulong, C. Songying, W. Dong, *Appl. Catal. A* 139 (1996) 75.
- [58] N.A. Dhas, A. Ekhtiarzadeh, K.S. Suslick, *J. Am. Chem. Soc.* 123 (2001) 8310.
- [59] F. Arena, R. Giovenco, T. Torre, A. Venuto, A. Parmaliana, *Appl. Catal. B* 45 (2003) 51.
- [60] J.W. Evans, M.S. Wainwright, A.J. Bridgewater, D.J. Young, *Appl. Catal.* 7 (1983) 75.
- [61] J. Agrell, H. Birgersson, M. Boutonnet, I. Melián-Cabrera, R.M. Navarro, J.L.G. Fierro, *J. Catal.* 219 (2003) 389.
- [62] A.A. Khassin, V.V. Pelipenko, T.P. Minyukova, V.I. Zaikovskii, D.I. Kochubey, T.M. Yurieva, *Catal. Today* 112 (2006) 143.
- [63] T.S. Askgaard, J.K. Nørskov, C.V. Ovesen, P. Stoltze, *J. Catal.* 156 (1995) 229.
- [64] I.A. Fisher, A.T. Bell, *J. Catal.* 172 (1997) 222.
- [65] F. Arena, G. Trunfio, E. Alongi, D. Branca, A. Parmaliana, *Appl. Catal. A* 266 (2004) 155.